Dark-field electron holography as a recording of crystal diffraction in real space: a comparative study with high-resolution X-ray diffraction for strain analysis of MOSFETs

Victor Boureau, Aurèle Durand, Patrice Gergaud, Delphine Le Cunff, Matthew Wormington, Denis Rouchon, Alain Claverie, Daniel Benoit, Martin Hÿtch

Boureau et al., J. Appl. Cryst. 53, 885-895 (2020). doi:10.1107/S1600576720006020

Dark-field electron holography as a recording of crystal diffraction in real space: a comparative study with high-resolution X-ray diffraction for strain analysis of MOSFETs

Victor Boureau,[a,b]* Aurèle Durand,[a,c] Patrice Gergaud,[c] Delphine Le Cunff,[a] Matthew Wormington,[d] Denis Rouchon,[c] Alain Claverie,[b] Daniel Benoit,[a] and Martin Hÿtch[b]

[a] STMicroelectronics, 850 rue Jean Monnet, 38926 Crolles Cedex, France.

[b] CEMES-CNRS, 29 rue Jeanne Marvig, 31055 Toulouse, France.

[c] Univ. Grenoble Alpes, CEA, LETI, F-38054 Grenoble, France.

[d] Bruker Semiconductor Division, 112 Robin Hill Road, Santa Barbara, CA 93117, USA.

* Correspondence e-mail: victor.boureau@epfl.ch

Abstract

Diffraction-based techniques, either with electrons or photons, are commonly used in material science to measure elastic strain in crystalline specimens. In this paper, we focus on two advanced techniques capable of accessing strain information at the nanoscale: high-resolution X-ray diffraction (HRXRD) and the transmission electron microscopy (TEM) technique of dark-field electron holography (DFEH). Both experimentally record an image formed by a diffracted beam: a map of the intensity in the vicinity of a Bragg reflection spot in the former and an interference pattern in the latter. The theory that governs these experiments will be described in a unified framework. The role of the geometric phase, which encodes the displacement field of a set of atomic planes in the resulting diffracted beam, is emphasised. A detailed comparison of experimental results acquired at a synchrotron and with a state-of-the-art TEM is presented for the same test structure: an array of dummy metal-oxide-semiconductor field-effect-transistors (MOSFETs) from the 22 nm technology node. Both techniques give access to accurate strain information. Experiment, theory and modelling allow us to illustrate the similarities as well as the inherent differences between the HRXRD and DFEH techniques.

Keywords

diffraction, elastic strain, geometric phase, dark-field electron holography (DFEH), high-resolution x-ray diffraction (HRXRD), metal-oxide-semiconductor field-effect-transistor (MOSFET)

1 – Introduction

The need for accurate nanoscale strain characterisation of crystalline materials and structures has been increasing steadily over recent years, driven notably by the microelectronics industry. Indeed, carrier mobility in semiconductors can be increased significantly through the introduction of strain (Fischetti & Laux, 1996). The consequential improvement in device performance is so significant that strain engineering has been an integral part of transistor technology since the 90 nm technology node (Song *et al.*, 2011). However, measuring strain at the nanoscale is not straightforward and has led to the development of several techniques using both X-rays and electrons.

In general, interplanar spacings, and hence strain, can be measured by X-ray diffraction (XRD) applying Bragg's law (Bragg & Bragg, 1913). For mapping strain at the submicron scale, scanning X-ray microdiffraction has been developed (Tamura *et al.*, 2003). The technique consists of recording the positions of strong crystal reflections while scanning the sample point by point. Nowadays, strain measurements with an accuracy of about 10^{-5} and a spatial resolution down to 100 nm can be realised with advanced focussing optics (Holt *et al.*, 2013). With another approach, high-resolution XRD (HRXRD) measures the intensity distribution in the vicinity of a strong reflection of the crystalline specimen, from which strain information can be retrieved (Eberlein *et al.*, 2008). When applied to a periodic structure illuminated with a beam that has a transverse coherence length that is larger than a few periods of the structure, a coherent diffraction pattern is observed and strain information relating to the averaged repeating unit is obtained (Minkevich *et al.*, 2014). More recently Bragg coherent diffractive imaging (CDI) techniques have been developed, where inversion algorithms are applied to fully coherent diffraction patterns to solve the phase problem and obtain strain maps with a spatial resolution of a few nanometres (Robinson & Harder, 2009; Yau *et al.*, 2017).

On the other hand, transmission electron microscopy (TEM) based techniques are widely used for nanometre spatial resolution measurements (Hÿtch & Minor, 2014). The main techniques based on electron diffraction are convergent-beam electron diffraction (CBED) (Zhang *et al.*, 2006), nano-beam electron diffraction (NBED) (Béché *et al.*, 2009), precession electron diffraction (PED) (Rouvière *et al.*, 2013) and dark-field electron holography (DFEH) (Hÿtch *et al.*, 2008). CBED, NBED and PED use an electron probe that scans the sample point by point recording diffraction patterns which are then

analysed similarly to X-ray microdiffraction. DFEH records an interference pattern in real space, using a coherent electron beam, from which the strain information is extracted by image processing.

Strain mapping techniques using X-rays and electrons are, however, rarely compared even though the underlying physics is very similar. In this study, we would like to address this point by drawing a close parallel between the specific techniques of HRXRD and DFEH, both theoretically and experimentally. The theory describing the physics of these experiments will be developed in a unified framework. A detailed comparison will follow of experimental results acquired with a synchrotron light source and with a state-of-the-art TEM for a test structure consisting of an array of strained metal-oxide-semiconductor field-effect-transistors (MOSFETs). Finally, the similarities and the main differences between these two techniques will be discussed.

2 – Experimental

2.1 – Specimen

The specimen, depicted in Figure 1(a), is an array of dummy p-type bulk MOSFETs derived from the 22 nm technology node. It is fabricated on a Si (001) 300 mm wafer and stopped before the silicidation steps (Cooper *et al.*, 2010). The devices were homogeneously patterned over a large 350 x 150 µm² rectangular area, the width of the area corresponding to the width of the dummy MOSFETs (y-direction). The individual devices have a 108 nm pitch in the x-direction, with a channel length of 20 nm, as shown in Figure 1(b). The first step was to realise the grid stack by the growth of the following layers successively on the substrate: SiO_2, high-permittivity HfO_2 oxide, TiN metal, followed by poly-Si and amorphous SiN deposits. Raised $Si_{0.7}Ge_{0.3}$ sources and drains (S/D) were then grown by reduced pressure chemical vapour deposition (RPCVD) epitaxy, and are separated from the grid by SiN spacers. They have a rectangular section of 67 x 35 nm². The respective lattice parameters are 0.5431 nm for Si and 0.5493 nm for $Si_{0.7}Ge_{0.3}$ (Dismukes *et al.*, 1964), resulting in a mismatch of 1.14% of the S/D relative to the Si substrate. A succession of stacking faults along {111} planes at the top corners of the S/D can be noticed (see Figure 1(b)). The (x, y, z) coordinate system identified in Figure 1, respectively along the $([110], [\bar{1}10], [001])$ crystal directions of the material, is conserved throughout this study.

For the TEM experiments, the sample was thinned in the y-direction by focused ion beam (FIB), using a FEI Helios 600i. The surface was previously protected by an amorphous Pt deposition and backside milling was performed to avoid curtaining effects (Schwarz *et al.*, 2003). A lamella of uniform thickness of about 110 nm was obtained.

2.2 – HRXRD

The HRXRD setup is sketched in Figure 2(a) and extensively detailed in (Pietsch *et al.*, 2004). It consists of recording diffraction patterns from the Fraunhofer diffraction of an X-ray beam, in the vicinity of a Bragg reflection of a crystalline specimen. The term "high-resolution" means that two or three dimensional (2D or 3D) reciprocal space maps (RSMs) are recorded from the diffracted beam, with sufficient sampling in the reciprocal space to allow detailed analysis of the intensity distribution. HRXRD experiments are non-destructive and 2D RSMs are now performed on product wafers within secondary manufacturing lines using conventional X-ray sources (Durand *et al.*, 2017).

In this work, however, HRXRD experiments were carried out at a synchrotron. The 33-BM-C beamline of the Advanced Photon Source (APS) equipped with a vertically collimating mirror, Si (111) double-crystal monochromator, vertically focussing mirror, a four-circle diffractometer and a hybrid pixel array detector (Pilatus 100K) located at a distance of 1 m from the sample was used at 27.17° Bragg angle (Karapetrova *et al.*, 2011). The X-ray energy was 10 keV and the beam was focused on a 100 x 100 µm² area of the sample. The footprint of the beam was centred on the homogeneously patterned area to avoid any strain relaxation occurring close to the edges (see Figure 1(a)). The strained structure is consequently considered as perfectly periodic in the (xz) observation plane and invariant along the y-direction. The transverse coherence area of the beam is estimated to be a few µm², which is significantly larger than the period of the structure but significantly smaller than the area of the beam. A 3D acquisition around the 004 diffracted beam was performed by using multiple acquisitions at different angles of the sample and 2D detector. The acquisition was followed by a conversion of the measurement coordinates to reciprocal space and a 3D interpolation in order to obtain a regular grating of the reciprocal space. These data processing steps enable the 3D RSM to be perfectly sliced in the

$(Q_x Q_z)$ plane to obtain the 2D RSM of interest, where Q_x (respectively Q_z) axis of reciprocal space is aligned to the x (respectively z) axis of direct space.

2.3 – DFEH

DFEH consists of recording an interference pattern using a coherent electron beam inside a TEM, as sketched in Figure 2(b). For that, an electron biprism is used to deflect and overlap two parts of the beam. One part probes the crystalline region-of-interest whilst the other part is diffracted by an unstrained crystal with a well-known periodicity used as a reference area. An aperture located in the back-focal-plane of the objective lens allows a specific diffracted beam, g, to be selected associated with a (hkl) set of planes, in order to study the interference pattern of that specific beam. The specimen is oriented in two-beam condition in order to maximise the intensity of the considered diffracted beam.

DFEH experiments were performed on the I²TEM-Toulouse, a Hitachi HF-3300C TEM equipped with a cold-field emission gun and an image aberration corrector B-COR from CEOS (Snoeck *et al.*, 2014). Holography was performed at an accelerating voltage of 300 kV in Lorentz imaging mode, using a dedicated stage of the TEM located above the objective lens in order to use the objective lens as a high-quality Lorentz lens. In combination with the aberration corrector, this allows wide fields of view to be visualised whilst retaining a spatial resolution of 0.5 nm. To avoid Fresnel fringes (Harada *et al.*, 2004), two electrostatic biprisms were used to create the hologram, resulting in a hologram fringe spacing of 1.08 nm. Holograms were recorded for the 004 and 220 diffracted beams, on a 4k by 4k pixels CCD camera (Gatan USC1000), with 10 s exposure time and a sampling density of 0.1143 nm/pixel.

Dark-field electron holograms were processed using the software package HoloDark 1.3 (HREM Research Inc.), a plug-in for the image-processing environment DigitalMicrograph 3.0 (Gatan Inc.), in order to extract phase maps and then strain maps from these holograms. Finite element method (FEM) modelling was performed using the structural mechanics module of COMSOL Multiphysics software in order to simulate the experimental phase maps corresponding to the TEM specimen, including the thin-lamella elastic relaxations in the y-direction, and to retrieve the phase maps corresponding to the bulk specimen before thinning (Javon *et al.*, 2014).

3 – Theory

In this section, we aim to describe the intensity maps recorded by HRXRD and DFEH experiments in a unified framework. An elastic strain field is considered in a monocrystalline structure, distributed in the (xz) plane and invariant in the y-direction (see Figure 1). The kinematic diffraction description from coherent elastic scattering, neglecting thermal diffuse scattering and absorption, is used to describe the interaction of the specimen with a monochromatic progressive plane wave of unit amplitude, written in the time-independent form:

$$\Psi_0(\vec{r}) = e^{i2\pi\overrightarrow{k_0}.\vec{r}} \tag{1}$$

Ψ_0 is the incident wave function, $\vec{r}$ the position vector and $\overrightarrow{k_0}$ the incident wave vector, with $k = \frac{1}{\lambda}$ and λ the wavelength.

3.1 – HRXRD

The photon wave function scattered by a specimen, Ψ^X_{scat}, is obtained by solving the time-independent Schrödinger equation under the first-order Born approximation and written in the far-field (Fultz & Howe, 2013):

$$\Psi^X_{scat}\left(\vec{Q}, \overrightarrow{r'}\right) \approx \frac{e^{i2\pi\overrightarrow{k'}.\overrightarrow{r'}}}{\left|\overrightarrow{r'}\right|} . \frac{e^2}{mc^2} \int \rho(\vec{r})\, e^{-i2\pi\vec{Q}.\vec{r}} d^3r \tag{2}$$

$\overrightarrow{k'}$ is the scattered wave vector, $\vec{Q} = \overrightarrow{k'} - \vec{k}$ the scattering vector, $\overrightarrow{r'}$ the position vector of the scattered wave, e the electron charge, m the electron mass, c the speed of light in vacuum and ρ the electron charge density of the specimen. In the case of an assembly of atoms, one can write the electron charge density as a sum of independent atomic charge densities centred on the positions of the atoms $\overrightarrow{R_J}$:

$$\rho(\vec{r}) = \sum_j \rho_{at}\left(\vec{r} - \overrightarrow{R_J}\right) \tag{3}$$

In a crystal, atoms are organised periodically and their positions can be described as two independent sums. The first one describes the positions of each of the N unit cells of the crystalline specimen, $\overrightarrow{R_l}$, and the second is the position of the atoms inside each identical unit cell, $\vec{r_j}$. In addition, in the case of a

low-strained crystal satisfying elastic theory, one can consider that the strain bodily translates the crystal unit cells, without modifying their internal structure. Thus, elastic strain generates a displacement, $\overrightarrow{u_l}$, associated with each unit cells of the crystal. We obtain:

$$\rho(\vec{r}) = \sum_{l=1}^{N} \sum_{j} \rho_{at}\left(\vec{r} - \left(\overrightarrow{R_l} + \overrightarrow{u_l} + \overrightarrow{r_j}\right)\right) \tag{4}$$

By substituting Equation (4) in Equation (2) and defining $\overrightarrow{r'}$ equal to $\vec{r} - \left(\overrightarrow{R_l} + \overrightarrow{u_l} + \overrightarrow{r_j}\right)$, we obtain, as $\overrightarrow{r'}$ is independent from $\overrightarrow{R_l}$, $\overrightarrow{u_l}$ and $\overrightarrow{r_j}$:

$$\Psi_{scat}^{X}\left(\vec{Q}, \overrightarrow{r'}\right) = \frac{e^{i2\pi\overrightarrow{k'}.\overrightarrow{r'}}}{\left|\overrightarrow{r'}\right|} . \frac{e^2}{mc^2} \sum_{i=1}^{N} \sum_{j} \int \rho_{at}\left(\overrightarrow{r'}\right) e^{-i2\pi\vec{Q}.\overrightarrow{r'}} d^3r' \left(e^{-i2\pi\vec{Q}.\left(\overrightarrow{R_l}+\overrightarrow{u_l}+\overrightarrow{r_j}\right)}\right) \tag{5}$$

In this equation, the atomic X-ray scattering factor, f^X, is identified as:

$$f^X(\vec{Q}) = \frac{e^2}{mc^2} \int \rho_{at}\left(\overrightarrow{r'}\right) e^{-i2\pi\vec{Q}.\overrightarrow{r'}} d^3r' \tag{6}$$

The X-ray structure factor, $F^X(\vec{Q}) = \sum_j f^X(\vec{Q}) e^{-i2\pi\vec{Q}.\overrightarrow{r_j}}$, describes the scattering by a unit cell of the crystal. Therefore, Equation (5) can be rewritten as follows:

$$\Psi_{scat}^{X}\left(\vec{Q}, \overrightarrow{r'}\right) = \frac{e^{i2\pi\overrightarrow{k'}.\overrightarrow{r'}}}{\left|\overrightarrow{r'}\right|} . F^X(\vec{Q}) . \sum_{i} \gamma(\overrightarrow{R_l}) e^{-i2\pi\vec{Q}.\overrightarrow{u_l}} e^{-i2\pi\vec{Q}.\overrightarrow{R_l}} \tag{7}$$

In this equation, the positions of the unit cells of the finite crystal have been explicitly defined in the sum by the shape function, γ, being 1 inside the specimen and 0 outside. In this way, the discrete Fourier transform (FT) is recognised. The discrete FT can be converted into a continuous FT because the displacement field is continuous for elasticity theory. Finally, the wave function scattered by the specimen in Fraunhofer conditions is written:

$$\Psi_{scat}^{X}\left(\vec{Q}, \overrightarrow{r'}\right) = \frac{e^{i2\pi\overrightarrow{k'}.\overrightarrow{r'}}}{\left|\overrightarrow{r'}\right|} . F^X(\vec{Q}) . S(\vec{Q}) \otimes FT\left[e^{-i2\pi\vec{Q}.\vec{u}(\vec{r})}\right] \tag{8}$$

where $S(\vec{Q}) = FT[\gamma(\vec{r})]$ is the shape factor and $\otimes$ represents the convolution.

Now we aim to describe specifically the case of a HRXRD experiment, where a detector is used to record the intensity of a diffracted beam in the vicinity of a Bragg spot. Close to the peak, $\vec{Q} = \vec{g} + \vec{s}$, where $\vec{g}$ is the diffraction vector of the crystal plane in Bragg conditions and $\vec{s}$ the Bragg deviation

vector, with $\vec{g} \gg \vec{s}$. It follows that $\vec{s}.\vec{u}$ is negligible compared to $\vec{g}.\vec{u}$ and therefore the X-ray structure factor depends solely on $\vec{g}$, written F_g^X. Thus, based on Equation (8), the RSM intensity can be expressed as:

$$I^{RSM}(\vec{Q}) = \left|\Psi_{scat}^X\left(\vec{Q},\vec{r'}\right)\right|^2 \propto \left|F_g^X\right|^2.S^2(\vec{Q})\otimes\left|FT\left[e^{-i2\pi\vec{g}.\vec{u}(\vec{r})}\right]\right|^2 \quad (9)$$

This equation shows that the displacement field of the specimen appears in the description of RSM intensity via a phase factor written:

$$\varphi^G(\vec{r}) = -2\pi\vec{g}.\vec{u}(\vec{r}) \quad (10)$$

where φ^G is called the geometric phase and contains the atomic displacement field $\vec{u}$ of the (hkl) set of atomic planes associated with the diffraction vector $\vec{g}$.

In HRXRD experiments, the geometric phase and hence the displacement field, is encoded directly in the phase of the diffracted beam as shown by Equation (8). However, since it is the intensity of the beam that is recorded as described by Equation (9), the phase is lost, leading to the well-known phase problem. Nevertheless, the geometric phase term still influences the recorded intensity but in a more indirect way.

3.2 – DFEH

The wave function of fast electrons interacting with a specimen, Ψ^e, is obtained by solving the time-independent Schrödinger equation, by using Wentzel-Kramers-Brillouin (WKB) approximation, and is written at the exit plane of the specimen as (Zuo & Spence, 2017):

$$\Psi_{exit}^e(\vec{r}) \approx \Psi_0(\vec{r}).e^{i\sigma\int V(\vec{r})dy} \quad (11)$$

y is chosen as the direction of propagation of the electron beam for consistency with our experimental results (see Figure 1(b)), V is the electrostatic potential of the specimen and $\sigma = \frac{2\pi me\lambda}{h^2}$ is the interaction constant with λ the relativistic electron wavelength and h the Planck constant. Equation (11) considers a perfect imaging system, with no optical aberrations, and stays valid in the image plane of the TEM which is conjugated with the exit plane of the specimen. The atomic periodic potential of a perfect crystal can be expanded into a Fourier series (Reimer & Kohl, 2008):

$$V(\vec{r}) = \sum_{g} V_g e^{i2\pi\vec{g}.\vec{r}} \tag{12}$$

$\vec{g}$ are the reciprocal lattice vectors of the crystal and V_g their Fourier components related to the electronic structure factor, $F_g^e = \frac{2\pi meV_c}{h^2} V_g$, where V_c is the volume of the unit cell. In the case of a low strained crystal satisfying linear elastic theory, the atomic lattice can be described by the unstrained crystal lattice being bodily translated by a small displacement $\vec{u}$ (Hÿtch *et al.*, 2011):

$$V(\vec{r}) = V_0 + \sum_{g\neq 0} V_g e^{i2\pi\vec{g}.(\vec{r}-\vec{u}(\vec{r}))} \tag{13}$$

V_0 is the mean inner potential (MIP) of the crystal. By substituting Equation (13) into Equation (11), we obtain:

$$\Psi_{exit}^e(\vec{r}) = \Psi_0(\vec{r}).\, e^{i\sigma\int V_0 dy} e^{i\sigma\int \sum_{g\neq 0} V_g e^{i2\pi\vec{g}.(\vec{r}-\vec{u}(\vec{r}))} dy} \tag{14}$$

Applying the weak phase object (WPO) approximation, we expand the second exponential of Equation (14) to first order:

$$\Psi_{exit}^e(\vec{r}) \approx \Psi_0(\vec{r}).\, e^{i\sigma\int V_0 dy}\left(1 + i\sigma\int \sum_{g\neq 0} V_g e^{i2\pi\vec{g}.(\vec{r}-\vec{u}(\vec{r}))}\, dy\right) \tag{15}$$

We are now in a position to describe specifically the DFEH experiment. The two-beam experimental condition allows us to consider solely one diffracted beam. Moreover, the DFEH setup uses an objective aperture in the back-focal-plane of the objective lens (see Figure 2(b)) to select the beam diffracted by a specific set of atomic planes, thus:

$$\Psi_g^e(\vec{r}) = \Psi_0(\vec{r}).\, e^{i\sigma\int V_0 dy}\left(i\sigma\int V_g e^{i2\pi\vec{g}.(\vec{r}-\vec{u}(\vec{r}))} dy\right) \tag{16}$$

For simplicity, we consider the strain field invariant over the y-direction, i.e. we neglect the relaxation effects over the constant thickness, t, of the TEM sample. Finally, the wave function of the diffracted beam can be written in the image plane, for a DFEH experiment:

$$\Psi_g^e(\vec{r}) \approx \Psi_0(\vec{r}).\frac{i\pi t}{\xi_g} e^{i2\pi\vec{g}.(\vec{r}-\vec{u}(\vec{r}))}.\, e^{i\sigma V_0 t} \tag{17}$$

where $\xi_g = \frac{\pi}{\sigma V_g}$ is the extinction distance associated with the diffracted beam g. The hologram intensity recorded from a DFEH setup is described as (Völkl *et al.*, 2013):

$$I^{DFEH}(\vec{r}) = \left|\Psi_g^e(\vec{r}) + \Psi_{g,ref}^e(\vec{r})\right|^2 = {A_g}^2(\vec{r}) + {A_{g,ref}}^2(\vec{r}) + 2\mu A_g(\vec{r})A_{g,ref}(\vec{r}).\cos\left(2\pi\overrightarrow{q_h}.\vec{r} + \Delta\varphi(\vec{r})\right) \quad (18)$$

where Ψ_g^e and $\Psi_{g,ref}^e$ are the parts of the electron wave emerging from the region-of-interest and the reference region in the sample, respectively (see Figure 2(b)). The hologram contrast is designated by μ and $\overrightarrow{q_h}$ is the carrier frequency resulting from the biprism-induced tilt between the two parts of the wave, $\Delta\varphi = \varphi_s - \varphi_{ref}$ is the phase shift between the two wave fronts. Amplitude and phase terms of Equation (18) are identified from Equation (17) as:

$$A_g(\vec{r}) = \frac{\pi t}{\xi_g}\gamma(\vec{r}) \quad (19)$$

and

$$\varphi_g(\vec{r}) = \frac{\pi}{2} + 2\pi\vec{g}.\vec{r} - 2\pi\vec{g}.\vec{u}(\vec{r}) + \sigma V_0 t \quad (20)$$

In Equation (19), the shape function of the crystal was introduced to describe the location where the specimen fulfils the g-Bragg diffraction condition, $\gamma = 1$, otherwise $\gamma = 0$. By substitution of these amplitude and phase terms in Equation (18), considering that the reference beam is diffracted by an unstrained crystal ($\overrightarrow{u_{ref}} = 0$) covering the whole field of view ($\gamma_{ref} = 1$), we obtain the following hologram intensity recorded during a DFEH experiment:

$$I^{DFEH}(\vec{r}) = \frac{\pi^2 t^2}{{\xi_g}^2}\left(1 + \gamma(\vec{r})\right) + 2\mu\frac{\pi^2 t^2}{{\xi_g}^2}\gamma(\vec{r}).\cos[2\pi\overrightarrow{q_h}.\vec{r} - 2\pi\vec{g}.\vec{u}(\vec{r})] \quad (21)$$

From the hologram intensity described in Equation (21), one can extract the phase and amplitude of the beam, encoded in the hologram, using Fourier processing (Völkl *et al.*, 2013). In the case of our study, the numerical complex FT of the hologram intensity is:

$$FT[I^{DFEH}(\vec{r})] = I^{DFEH}(\vec{q}) = FT\left[\frac{\pi^2 t^2}{{\xi_g}^2}\left(1 + \gamma(\vec{r})\right)\right] + \delta(\vec{q} + \overrightarrow{q_h}) \otimes FT\left[\mu\frac{\pi^2 t^2}{{\xi_g}^2}\gamma(\vec{r})e^{-i2\pi\vec{g}.\vec{u}(\vec{r})}\right] + \delta(\vec{q} - \overrightarrow{q_h}) \otimes FT\left[\mu\frac{\pi^2 t^2}{{\xi_g}^2}\gamma(\vec{r})e^{i2\pi\vec{g}.\vec{u}(\vec{r})}\right] \quad (22)$$

where $\vec{q}$ is the reciprocal position vector of the FT and δ the Dirac delta function. It then becomes simple to use a numerical aperture in reciprocal space to select the signal in the vicinity of the carrier frequency, described as:

$$I_{q_h}^{DFEH}(\vec{q}) = \mu \frac{\pi^2 t^2}{{\xi_g}^2} . S(\vec{q}) \otimes FT\left[e^{-i2\pi \vec{g}.\vec{u}(\vec{r})}\right] \tag{23}$$

Next a numerical inverse FT is performed to retrieve the following complex image:

$$I_{complex}^{DFEH}(\vec{r}) = FT^{-1}\left[I_{q_h}^{DFEH}(\vec{q})\right] = \mu \frac{\pi^2 t^2}{{\xi_g}^2} \gamma(\vec{r}) e^{-i2\pi \vec{g}.\vec{u}(\vec{r})} \tag{24}$$

Finally, the phase and amplitude images are extracted from this complex image.

Equation (24) shows that, after a straightforward processing of dark-field holograms, the geometric phase described in Equation (10) is spatially mapped across the specimen. This previous development proves that φ^G, thus the atomic displacement field, is directly accessible via DFEH at any point in the specimen. Furthermore, the crystal strain field can be calculated by the gradient of this displacement field:

$$\varepsilon_{ij} = \frac{1}{2}\left(\frac{\partial u_i(\vec{r})}{\partial r_j} + \frac{\partial u_j(\vec{r})}{\partial r_i}\right) \tag{25}$$

where the index numbers i,j represent $[hkl]$ crystal directions and $u_{i,j}$ is the displacement field associated with the (hkl) planes. Thus the 2D strain tensor of the specimen can be obtained with two DFEH measurements, from two non-collinear diffracted beams (Hÿtch *et al.*, 2011).

It should be noted, however, that this theoretical development assumes the WPO approximation and that no strain relaxation has occurred in the TEM thin-lamella specimen. A more accurate treatment consists of describing the dynamical diffraction of the transmitted and diffracted beam, as developed in (Lubk *et al.*, 2014), and calculating the thin-film relaxation. This refinement will be considered in next section, in order to retrieve the geometric phase maps of the bulk specimen before thinning by using FEM modelling (Javon *et al.*, 2014).

4 – Results

4.1 – HRXRD

Figure 3 shows the RSM in the $(Q_x Q_z)$ plane, acquired in the vicinity of the 004 diffracted beam. A certain amount of strain information can be easily extracted from such RSMs of periodic structures (Medikonda *et al.*, 2014). We observe a signal from two distinct regions in the RSM shown in Figure 3: an upper region around $Q_z = 7.365$ nm^{-1} and a lower one around $Q_z = 7.245$ nm^{-1}. The former corresponds to a lattice interplanar distance of $\frac{1}{Q_z} = 0.1358$ nm, equal to the bulk spacing of the (004) Si and can thus be associated with the Si substrate. The latter corresponds to an interplanar distance of about 0.1380 nm and can be associated with the SiGe S/D. Indeed, incorporation of Ge in Si increases the lattice parameter (Dismukes *et al.*, 1964). It is therefore straightforward to calculate the out-of-plane deformation of the S/D relative to the relaxed bulk Si reference, of 1.63%.

In the Si region, we observe a very intense and sharp peak. This results from the deep penetration of the X-rays below the strained structure and corresponds to the unstrained bulk Si substrate. More significantly, the RSM has a periodic intensity modulation in the Q_x direction, present in both the Si and SiGe regions of the RSM. This phenomenon arises from periodic distributions along the x-direction of the specimen. Both the shape factor $\gamma(\vec{r})$ and strain $\vec{u}(\vec{r})$ are periodic functions with a period p whose Fourier transforms are also periodic with a period p^{-1}, as seen in Equation (9). p^{-1} is measured close to 0.009 nm^{-1} in the RSM, which corresponds to a strain periodicity of 111 nm in the sample. In fact, the pitch of the sample (repeating units every 108 nm) imposes the same periodicity on the strain field.

4.2 – DFEH

Figure 4 shows the results from the DFEH measurement. Figure 4(a) displays the dark-field hologram acquired using the 004 diffracted beam. The initially recorded image has been rotated and cropped, to show exactly 3 repeating units of the structure. The hologram has a fringe contrast of 13% in the crystalline part of the sample. Figure 4(b) shows the geometric phase encoded in the fringe displacement, extracted with standard Fourier processing, as described by Equation (22). The radius of the numerical aperture used in the Fourier space limits the spatial resolution of the phase image to 4 nm, which is sufficient for our purposes. The regions corresponding to the amorphous parts of the sample have been blanked out in the phase image (see Figure 4(b)) since they diffract diffusely and consequently

contain no interpretable strain information. Figure 4(c) is the displacement field of the (004) crystal planes, calculated from the geometric phase described in Equation (10). Figure 4(d) is the strain field of the (004) planes, which derives from the displacement field as shown in Equation (25). Globally, Figure 4 illustrates the ability of DFEH technique to map the strain field of an epitaxial system, in an unequivocal way, via the geometric phase encoded in the hologram. DFEH gives access to a detailed strain map with a strain sensitivity of 5.10^{-4}, estimated in this study from the standard deviation of the strain fluctuations in the region of the substrate where no strain should be present.

The many details of the strain field can be appreciated in Figure 4(d). The complex distribution results from the multiple process steps used for the fabrication of the array of MOSFETs. The principal aspects result from the high compressive stress of the as-deposit TiN metal grid and from the SiGe S/D epitaxy (Boureau *et al.*, 2018). We observe an identical periodicity for the strain distribution as for the structure, as expected from symmetry considerations. The strain distribution can be separated into two distinct areas: within the S/D and within the Si substrate over a distance of about 100 nm from the surface.

A large out-of-plane strain (ε_{zz}) can be seen in the S/D, measured to be about 1.65% at the centre, and decreasing to 1.05% close to the edge. Note that, as for HRXRD, the strain within the source and drain regions refers to the deformation of the local lattice with respect to the Si substrate. It is distinct from the elastic strain which is measured with respect to the relaxed lattice parameter of the SiGe. The mismatch being 1.14%, the Poisson reaction extends by 0.5% the SiGe lattice in the out-of-plane direction with respect to its lattice parameter in the bulk. The reason is that the SiGe is grown in perfect epitaxy and initially matches the in-plane Si lattice parameter, meaning that the SiGe is highly compressed in both in-plane directions (i.e. by -1.14%). Away from the interface with the substrate, the SiGe can progressively relax due to the proximity of the lateral interfaces with the gate and the free surface in the growth direction.

Within the Si substrate, there is little possibility to relax the stresses and we observe an intricate distribution of strain. Just below the gate, the silicon is in tension, whereas deeper into the substrate the silicon is in compression. Between the gates, this distribution inverts. Globally, the dominating effects observed in the strain distribution result from the compressive TiN gate stressor in the region close to

the surface of the silicon substrate and from the compressive SiGe S/D stressors deeper into the substrate.

4.3 – Experimental comparison of DFEH and HRXRD

It is difficult to compare directly DFEH and HRXRD measurements as depicted in Figures 3 and 4, as the former is recorded in real space and the latter in reciprocal space. However, there are elements of similarity. For instance, it was shown previously that both measurements exhibit the same strain periodicity and that they both measure similar strains corresponding to the SiGe S/D regions. On the other hand, the ability of DFEH to map the displacement field in real space explains certain features of the HRXRD measurement, as for example the crescent shape of the S/D area in the experimental RSM shown in Figure 3. The strain is maximal at the middle of this shape, at $Q_x = 0$ nm^{-1} with the lower Q_z. It corresponds to the centre of the S/D region revealed by DFEH in Figure 4(d). Next, while $|Q_x|$ increases in the RSM of Figure 3, the crescent shape describes a decrease of Q_z. This shape results from bending of the (004) planes as they approach the edges of the S/D, as visible in the DFEH map of the displacement field in Figure 4(c). Thus $|Q_x|$ increases close to the S/D edges. This effect is associated with a lower strain close to the S/D edges, as shown in the DFEH strain map in Figure 4(d). Thus Q_z increases close to the S/D edges. In the end the crescent shape of the HRXRD RSM is well explained by the DFEH maps, with regard to the local strain information.

In order to provide a more precise comparison of the results obtained from these two techniques, we need to express the two set of measurements in a similar way. Ideally, we would compare the atomic displacement fields but for HRXRD, these cannot be determined directly from the data. We therefore base our comparison on RSMs, the experimental HRXRD RSM and an RSM generated from the displacement field measured by DFEH (Durand *et al.*, 2015). Briefly, a 2D atomistic model of the (xz) plane of three repeating units of the structure is built for this purpose. Atomic positions of the perfectly unstrained Si crystal are generated inside the shape of the structure as determined by TEM imaging (see Figure 1(b)) and then refined with respect to the displacement field as measured by DFEH. In this way, we used the displacement field of the (004) planes (shown in Figure 4(c)) as well as the (220) planes displacement (not shown) in order to generate the atomic positions for the model. The Fraunhofer

diffraction pattern of the atomistic model is then computed with DeusX software (Durand, 2016), in the vicinity of the 004 diffracted beam, using Equation (5). The results are shown in Figure 5.

First, we compare Figure 5(a) with the experimental HRXRD RSM in Figure 3. Qualitatively, they are very similar both in the main peak coming from the silicon substrate and in the crescent-shaped set of diffraction spots coming from the SiGe. However, in the DFEH-generated RSM, the crescent is closer to the silicon peak. This can be seen more clearly in Figure 5(c) where the maxima of the peak positions in Q_z have been measured and plotted as a function of Q_x. In other words, there is a reduction in the out-of-plane strain of the S/D measured by DFEH. The reason is well known in electron microscopy experiments. In order to make specimens transparent to electrons, they must be thinned down in the observation direction, to about 110 nm in our case. The introduction of two free surfaces allows the sample to elastically relax in the y-direction with respect to the bulk. Interestingly, one can link the position of the maximum of the main SiGe satellite peak of the RSM directly generated from DFEH measurement (Figure 5(a)) to the DFEH strain measurement (Figure 4(d)). It corresponds to the value of the strain that matches the largest volume of the SiGe for the conditions where $Q_x = 0$ nm^{-1}, i.e. where no bending of the (004) planes occurs (see Figure 4(b)). Indeed, the maximum of the histogram of the DFEH strain measurement plotted from this area shows a strain of 1.17%, in good agreement with the position of $Q_z = 7.278$ nm^{-1} plot in Figure 5(c), corresponding to a strain of 1.18%.

In order to correct for the thin-lamella relaxation, we need to model the strain field. For this, we use a FEM model to simulate strain in the thin specimen as observed by TEM. The deformation measured by DFEH is, however, a 2D projection of the 3D structure and requires a sophistication of the FEM model to take into account the effects of two-beam dynamical diffraction (Javon *et al.*, 2014). In particular, the contribution of the geometric phase along the direction of propagation of the TEM electron beam in the sample (y-direction) is weighted. A limited number of parameters of the structural mechanics model, namely the as-deposit stresses of the gate materials, are then refined to reproduce the experimental DFEH strain measurements. Once a satisfactory model has been obtained for the thin lamella, we simply modify the boundary conditions of the FEM model to obtain the displacement field of the sample before thinning.

Figure 5(b) shows the RSM generated from DFEH measurements, after correction for the thin-lamella relaxation effects. The crescent shape is now further away from the Si peak (see Figure 5(c)) than in the RSM directly generated from DFEH measurements (plotted in Figure 5(a)). The Q_z position of the main peak of the SiGe S/D moves from 7.278 nm^{-1} to 7.245 nm^{-1}, suggesting a thin-lamella relaxation of 27% in the S/D. It is interesting to note that the spots themselves are less extended in the Q_z-direction of the DFEH-generated RSM after correction of the thin-lamella relaxation (Figure 5(b)). This is undoubtedly due to the fact that the lamella allows a greater range of out-of-plane deformations as the strain relaxes towards the free surfaces. In the FEM model corrected for thin-lamella relaxation, on the other hand, the strains do not vary in the projection direction (y-axis).

Now, by means of the RSMs shown in Figures 5(b) and 3, it becomes easier to compare the results from DFEH and HRXRD experiments. Indeed, we observe an excellent match between the HRXRD RSM and the DFEH-generated RSM corrected for thin-lamella relaxation. Quantitatively, this is confirmed by the positions of the diffraction spots shown in Figure 5(c). The DFEH and HRXRD spots from SiGe S/D are now almost exactly superposed.

5 – Discussion

The results so far have illustrated the ability of DFEH and HRXRD to extract similar strain information from a crystalline specimen. This is perhaps not surprising as both techniques result from the coherent diffraction of a specific set of atomic planes. They both record information from a single diffracted beam in Bragg condition and its immediate vicinity, either with a partially coherent X-ray beam for HRXRD or a coherent fast electron beam for DFEH. We have already outlined the theory to describe these experiments.

The experimental results also show that DFEH encodes the same information as HRXRD, by the means of a comparison of RSMs. However, two notable differences are identified and easily explained in the following. The first one concerns the higher intensity of the relaxed Si peak of the HRXRD RSM, located at the $Q_x = 0$ nm^{-1}, $Q_z = 7.365$ nm^{-1} position. The displacement field used to generate the RSMs from DFEH measurements extends to a depth of 300 nm into the silicon substrate, which was sufficient to contain all of the strained region-of-interest (see Figure 4(d)) but was much smaller than

the X-ray penetration depth in the Si substrate of about 140 µm (Grodstein, 1957). Thus an intense peak located at the position of the relaxed Si is recorded by HRXRD, in Figure 3. The second concerns the smaller signal-to-noise ratio of the HRXRD RSM. This RSM obviously includes measurement noise and thermal diffuse scattering of the sample, resulting in a diffuse background in the HRXRD RSM. The RSM generated from a DFEH experiment, in Figure 5(b), has no measurement noise since the measured displacement field has been reproduced by a FEM model, and no thermal diffuse scattering noise since the generation of the RSM does not take this phenomenon into account.

Further discussion of the approximations we used in the theory section will clarify the similarities and differences between the results from these two techniques. As the strained structure is localised within 150 nm of the surface, the dynamical diffraction of X-rays can be neglected. X-ray dynamical effects only occur for the intense Si peak but this signal comes from deep in the substrate where no strain exists and do not influence the RSM around this specific location. Thus Equation (8) describes well the X-ray wave in the far-field after diffraction by the sample. In the case of DFEH, the sample is oriented in two-beam condition for the 004 diffracted beam. The sample is 110 nm thick and the extinction distance of the 004 diffracted beam in Si is only 188 nm for the electron energy we used. Indeed, electrons are charged particles and interact more strongly with materials than X-rays. Hence the dynamic theory in two-beam condition should be applied, as discussed previously. It leads to a weighting of the geometric phase contribution of the exit wave function of the diffracted beam as the beam crosses the sample (Lubk *et al.*, 2014). The modification of Equation (17) is only slight, so it still describes to a good approximation the electron wave diffracted by a thin specimen in the image plane. Equations (8) and (17) show that the information of interest, namely the atomic displacement field, is encoded in the phase of the wave description and appears under the geometric phase expression described in Equation (10).

HRXRD records directly the far-field X-ray diffraction pattern in the vicinity of a Bragg spot, or RSM, as described by Equation (9). As a detector is sensitive to the beam intensity, the RSMs give access to the amplitude of the beam while its phase is lost. This phenomenon is known as the phase problem. In fact, a map of the diffraction intensity is obtained, as shown in Figure 3, from which the strain distribution in real space is no longer directly accessible. Notwithstanding, a certain amount of

information about the strain can be deduced from the beam amplitude. Indeed, the diffraction intensity map records all the different values of the strain and local orientations of the crystalline specimen but unfortunately direct access to the spatial localisation associated with these values is lost. Interference effects, encoded in the phase factors such as the geometric phase, can modulate the intensity recorded in the RSM, giving information about the spatial distribution of the strain. Such effects are visible in Figure 3, like the modulation along the x-direction originating from the periodicity of the sample. The transverse coherence length of the beam is much larger than a few repeating units of the structure, allowing these interference effects to be observable in the RSM measured by HRXRD. To a certain extent, the phase problem can be overcome using sophisticated Bragg CDI methods by reconstructing the phase with an iterative algorithm based on recorded intensities (Diaz *et al.*, 2010; Minkevich *et al.*, 2014; Miao *et al.*, 2015), however the inversion is neither straightforward nor unambiguous (see Figure 6).

DFEH, on the other hand, records an interference pattern between two diffracted coherent electron beams in the image plane of the microscope. The recorded dark-field hologram intensity, outlined in Equation (21), encodes in real space the geometric phase term of the diffracted electron beam, described in Equation (17). Standard Fourier processing, described as follows and depicted in Figure 6, is used to retrieve the geometric phase map encoded in the fringes (cosine term of Equation (21)) of the hologram. A numerical complex FT is performed, corresponding to Equation (22), followed by an inverse FT centred on the carrier frequency of the hologram so that the complex image described in Equation (24) can be obtained. The phase is then extracted from the complex image, which corresponds to the phase encoded in the hologram intensity. Finally, the displacement and strain fields of the specimen are calculated from the geometric phase map using Equations (10) and (25), as shown in Figure 6.

Furthermore, the similarity between DFEH and HRXRD experiments can be even more directly observed by looking at the FT of the electron hologram, in the vicinity of the carrier frequency, shown in Figure 6. The resemblance to the HRXRD RSM is striking. In fact, the top-right image of Figure 6 depicts the intensity of the complex FT of the hologram in the vicinity of q_h, outlined by Equation (23). We recognise in this expression the same terms as those describing the HRXRD RSM intensity in

Equation (9). $\mu\frac{\pi^2 t^2}{{\xi_g}^2}$ is equivalent to the square of the structure factor of X-rays, $\left|F_g^X\right|^2$. Indeed, the extinction distance, ξ_g, is inversely proportional to the electron structure factor, $F_g^e = \frac{\pi V_c}{\lambda \xi_g}$. The main difference lies on the fact that HRXRD RSM gives access to the square of the shape factor and geometric phase factor (see Equation (9)), whereas the FT of the hologram depicts directly these two factors (see Equation (23)). Of course the sampling of these two images is significantly different. HRXRD records the RSM with a good spatial resolution of about 8.0 x 10^{-4} nm^{-1}, whereas in the case of the hologram FT the sampling is inversely proportional to the hologram field of view, and thus much worse. In our study, the hologram field of view is 546 nm, indicating a sampling of 2.14 x 10^{-3} nm^{-1}. In Figure 6, the hologram FT has been resampled to smooth the aliasing. In addition, thin-lamella relaxation effects are not corrected in the FT of the hologram, which has similar consequences as for the RSM generated directly from DFEH measurement, shown in Figure 5(a). Noise levels are not comparable as the major part originates from the depth of the Si substrate in the case of the HRXRD RSM, due to the huge penetration depth of X-rays. Whereas the noise only originates from the field of view of the hologram in the case of the DFEH experiment. Thus the hologram FT seems less noisy. Overall, a good agreement of shapes and intensities is observed between the HRXRD RSM and the FT of dark-field hologram, depicted in Figure 6.

6 – Conclusion

The theory of diffraction has been used to describe the intensities recorded by HRXRD and DFEH experiments. Both techniques are based on the same underlying physics, describing the beam diffracted by a strained crystal in Bragg condition. The information of interest, namely the atomic displacement field, is encoded in the geometric phase of the diffracted beam. Supported by experimental observations, we have shown that the intensity of the FT of the DFEH hologram, around the carrier frequency, is closely equivalent to the RSM intensity recorded during an HRXRD experiment. Indeed, we have shown that DFEH and HRXRD allow similar strain information to be extracted. DFEH records the diffracted electron beam in the real space and the shift of the hologram fringes is proportional to the geometric phase, and hence to the displacement field present in the sample (see Equation (21)). The FT of the

electron hologram, in the vicinity of the carrier frequency of the hologram, is thus equivalent to the FT of the diffracting lattice planes. HRXRD records the diffracted X-ray beam in the far-field, which also corresponds to the FT of the density of electrons of the diffracting set of atomic planes (Equation (2)). In both cases, the FT of the considered crystal planes position is obtained. However, the X-ray detector records the beam intensity and in so-doing loses the phase information, whereas the equivalent numerical FT of the electron hologram is complex and thus preserves the phase information. This specificity allows DFEH to map directly the geometric phase in real space, via Fourier processing, in order to access to the spatial distribution of the displacement field.

The quantitative comparison of results from TEM and X-ray diffraction experiments on the same specimen allowed the similarities and differences between HRXRD and DFEH experiments to be fully appreciated. The consistency of the results reveal that both techniques are sensitive to the same structural quantities. However, based on theory and experiment, we also emphasise the important differences, as summarised in Figure 6. Geometric phase is mapped in real space with DFEH, giving a direct access to the strain distribution, whereas for HRXRD this is not the case. However, as with all TEM strain measurement techniques, thin-lamella relaxation effects need to be considered. In this respect, the FEM modelling approach we have used to reconstruct RSMs is validated by the excellent agreement with the HRXRD measurements collected from the bulk, unrelaxed specimen. Therefore, DFEH can be used as a valuable tool to support non-destructive in-line metrology performed by HRXRD. X-ray Bragg CDI techniques may be used in order to bypass the phase problem and reconstruct the geometric phase from fully coherent RSMs but require the use of high-brightness synchrotron beamlines.

Acknowledgements

The authors acknowledge financial support the National Research Agency under the program “Investissement d’Avenir” reference No. ANR-10-38-01-EQPX. The research leading to these results has received funding from the European Union Horizon 2020 research and innovation programme under grant agreement No. 823717 – ESTEEM3. Use of the Advanced Photon Source was supported by the U.S. Department of Energy, Office of Science, Office of Basic Energy Sciences, under Contract No. DE-AC02-06CH11357.

References

Béché, A., Rouvière, J.-L., Clément, L. & Hartmann, J.-M. (2009). *Appl. Phys. Lett.* **95**, 123114.

Boureau, V., Benoit, D. & Claverie, A. (2018). *ECS J. Solid State Sci. Technol.* **7**, P473–P479.

Bragg, W. H. & Bragg, W. L. (1913). *Proc. R. Soc. Lond. Ser. Contain. Pap. Math. Phys. Character*. **88**, 428–438.

Cooper, D., Béché, A., Hartmann, J.-M., Carron, V. & Rouvière, J.-L. (2010). *Appl. Phys. Lett.* **96**, 113508.

Diaz, A., Chamard, V., Mocuta, C., Magalhães-Paniago, R., Stangl, J., Carbone, D., Metzger, T. H. & Bauer, G. (2010). *New J. Phys.* **12**, 035006.

Dismukes, J., Ekstrom, L. & Paff, R. (1964). *J. Phys. Chem.* **68**, 3021–3027.

Durand, A. (2016). DeusX software. http://aurele.eu/#softwares

Durand, A., Boureau, V., Lecunff, D., Hourtane, A., Benoit, D., Claverie, A., Hytch, M., Rouchon, D. & Gergaud, P. (2015). *2015 IEEE 15th International Conference on Nanotechnology (IEEE-NANO)*, Vol. pp. 785–788.

Durand, A., Kaufling, M., Le-Cunff, D., Rouchon, D. & Gergaud, P. (2017). *Mater. Sci. Semicond. Process.* **70**, 99–104.

Eberlein, M., Escoubas, S., Gailhanou, M., Thomas, O., Rohr, P. & Coppard, R. (2008). *Thin Solid Films*. **516**, 8042–8048.

Fischetti, M. V. & Laux, S. E. (1996). *J. Appl. Phys.* **80**, 2234–2252.

Fultz, B. & Howe, J. M. (2013). Transmission electron microscopy and diffractometry of materials Springer.

Grodstein, G. W. (1957). X-ray Attenuation Coefficients from 10 Kev to 100 Mev U.S. Department of Commerce, National Bureau of Standards.

Harada, K., Tonomura, A., Togawa, Y., Akashi, T. & Matsuda, T. (2004). *Appl. Phys. Lett.* **84**, 3229–3231.

Holt, M., Harder, R., Winarski, R. & Rose, V. (2013). *Annu. Rev. Mater. Res.* **43**, 183–211.

Hÿtch, M., Houdellier, F., Hüe, F. & Snoeck, E. (2008). *Nature*. **453**, 1086–1089.

Hÿtch, M. J., Houdellier, F., Hüe, F. & Snoeck, E. (2011). *Ultramicroscopy*. **111**, 1328–1337.

Hÿtch, M. J. & Minor, A. M. (2014). *MRS Bull.* **39**, 138–146.

Javon, E., Lubk, A., Cours, R., Reboh, S., Cherkashin, N., Houdellier, F., Gatel, C. & Hÿtch, M. J. (2014). *Ultramicroscopy*. **147**, 70–85.

Karapetrova, E., Ice, G., Tischler, J., Hong, H. & Zschack, P. (2011). *Nucl. Instrum. Methods Phys. Res. Sect. Accel. Spectrometers Detect. Assoc. Equip.* **649**, 52–54.

Lubk, A., Javon, E., Cherkashin, N., Reboh, S., Gatel, C. & Hÿtch, M. (2014). *Ultramicroscopy*. **136**, 42–49.

Medikonda, M., Muthinti, G. R., Fronheiser, J., Kamineni, V., Wormington, M., Matney, K., Adam, T. N., Karapetrova, E. & Diebold, A. C. (2014). *J. Vac. Sci. Technol. B.* **32**, 021804.

Miao, J., Ishikawa, T., Robinson, I. K. & Murnane, M. M. (2015). *Science*. **348**, 530–535.

Minkevich, A. A., Köhl, M., Escoubas, S., Thomas, O. & Baumbach, T. (2014). *J. Synchrotron Radiat.* **21**, 774–783.

Pietsch, U., Holý, V. & Baumbach, T. (2004). High-resolution X-ray scattering: From thin films to lateral nanostructures Springer.

Reimer, L. & Kohl, H. (2008). Transmission electron microscopy: Physics of image formation Springer.

Robinson, I. & Harder, R. (2009). *Nat. Mater.* **8**, 291–298.

Rouvière, J.-L., Béché, A., Martin, Y., Denneulin, T. & Cooper, D. (2013). *Appl. Phys. Lett.* **103**, 241913.

Schwarz, S. M., Kempshall, B. W., Giannuzzi1, L. A. & McCartney, M. R. (2003). *Microsc. Microanal.* **9**, 116–117.

Snoeck, E., Houdellier, F., Taniguch, Y., Masseboeuf, A., Gatel, C., Nicolai, J. & Hytch, M. (2014). *Microsc. Microanal.* **20**, 932–933.

Song, Y., Zhou, H., Xu, Q., Luo, J., Yin, H., Yan, J. & Zhong, H. (2011). *J. Electron. Mater.* **40**, 1584.

Tamura, N., MacDowell, A. A., Spolenak, R., Valek, B. C., Bravman, J. C., Brown, W. L., Celestre, R. S., Padmore, H. A., Batterman, B. W. & Patel, J. R. (2003). *J. Synchrotron Radiat.* **10**, 137–143.

Völkl, E., Allard, L. F. & Joy, D. C. (2013). Introduction to electron holography Springer Science & Business Media.

Yau, A., Cha, W., Kanan, M. W., Stephenson, G. B. & Ulvestad, A. (2017). *Science*. **356**, 739–742.

Zhang, G., Istratov, A. A., Weber, E. R., Kiseilowski, C., He, H., Nelson, C. & Spence, J. H. C. (2006). *Appl. Phys. Lett.* **89**, 161907.

Zuo, J. M. & Spence, J. H. C. (2017). Advanced transmission electron microscopy: Imaging and diffraction in nanoscience Springer.

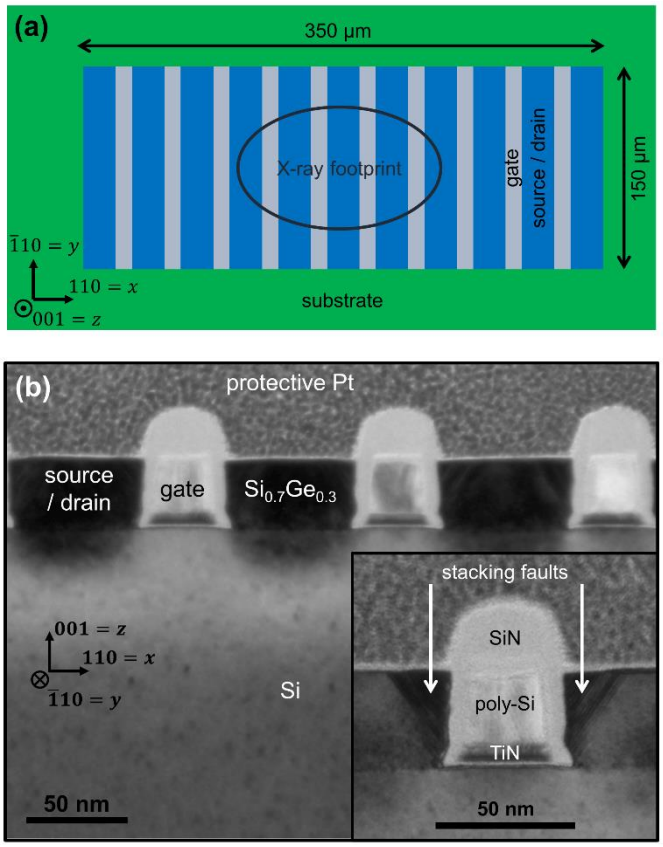

Figure 1: (a) Schematic top view of the periodic strained structure where the axis and the position of the X-ray footprint for HRXRD measurements are shown. (b) Cross-section bright-field TEM image of three repeating units of the array of dummy p-MOSFETs and enlargement of the gate structure inset. The materials, stacking faults at the top corners of S/D and crystallographic orientation are specified.

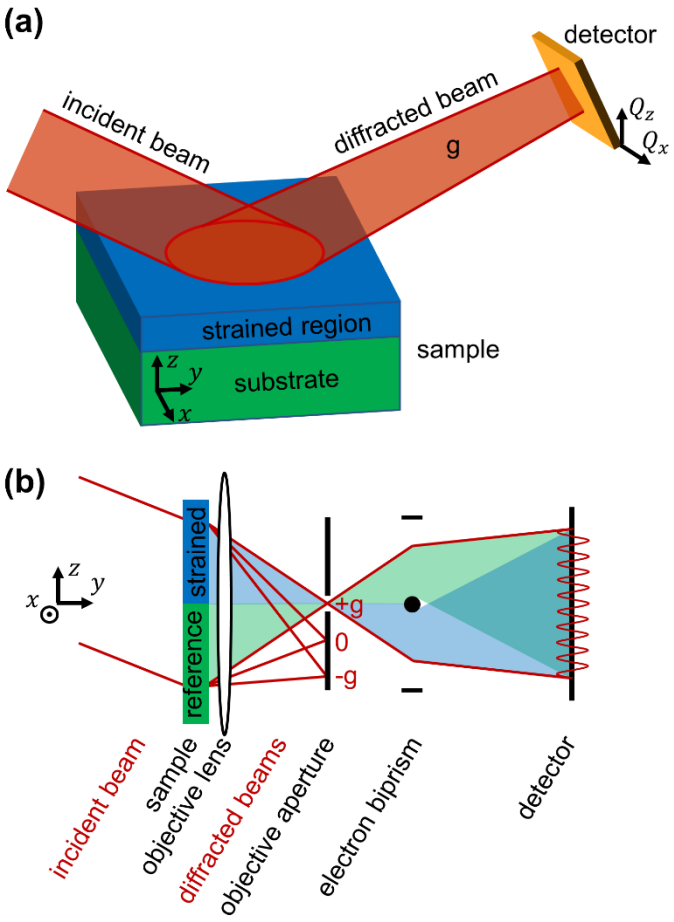

Figure 2: Schematic diagrams of (a) HRXRD and (b) DFEH experiments and coordinate system used in our study. The strained region-of-interest is highlighted in blue while the unstrained crystal substrate is in green. Here, the usual representation of DFEH is rotated 90° for a better comparison of both optical setups.

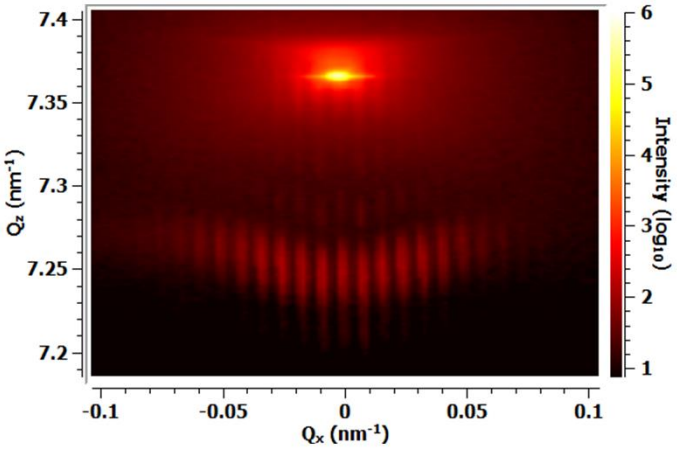

Figure 3: Experimental RSM of the 004 diffracted beam in the $(Q_x Q_z)$ plane, acquired by HRXRD with a synchrotron X-ray beam.

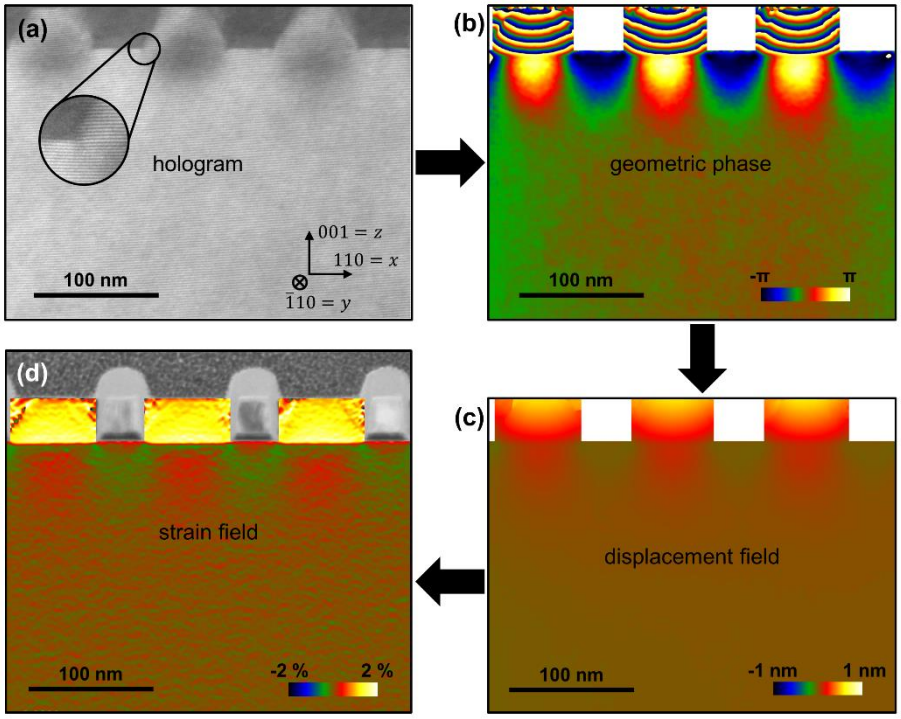

Figure 4: (a) Dark-field hologram of 3 repeating units of the MOSFETs structure using the 004 diffracted beam and enlargement inset allowing the visualisation of interference fringes. (b) Geometric phase map extracted from the hologram using the usual Fourier reconstruction. Amorphous part of the sample has been blanked out. (c) Displacement field of the (004) crystal planes calculated from the geometric phase and (d) the resulting out-of-plane strain field, ε_{zz}, superimposed on the bright-field TEM image in the amorphous part of the structure.

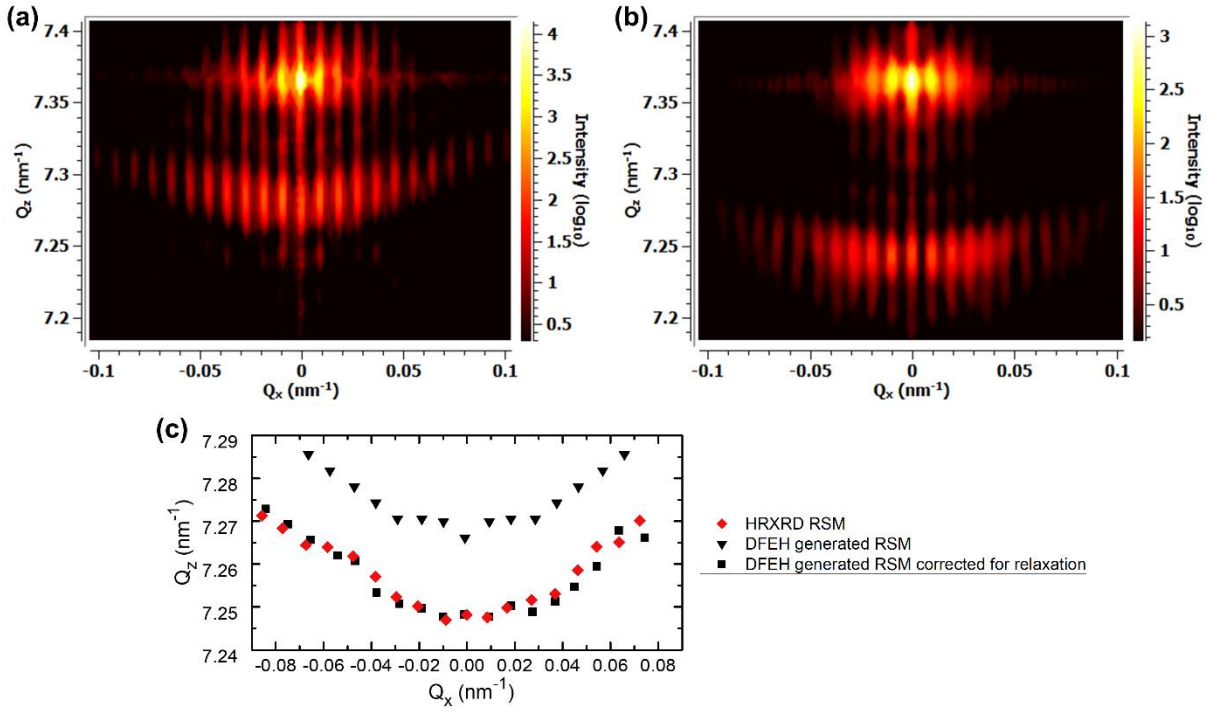

Figure 5: RSMs generated by using the displacement field measured by DFEH (a) before and (b) after correction of thin-lamella relaxation effects by FEM modelling. (c) Plot of the maxima positions of the SiGe S/D satellite spots from the three RSMs, measured by HRXRD (Figure 3) and generated from DFEH measurements before (Figure 5(a)) and after (Figure 5(b)) correction of the thin-lamella relaxation.

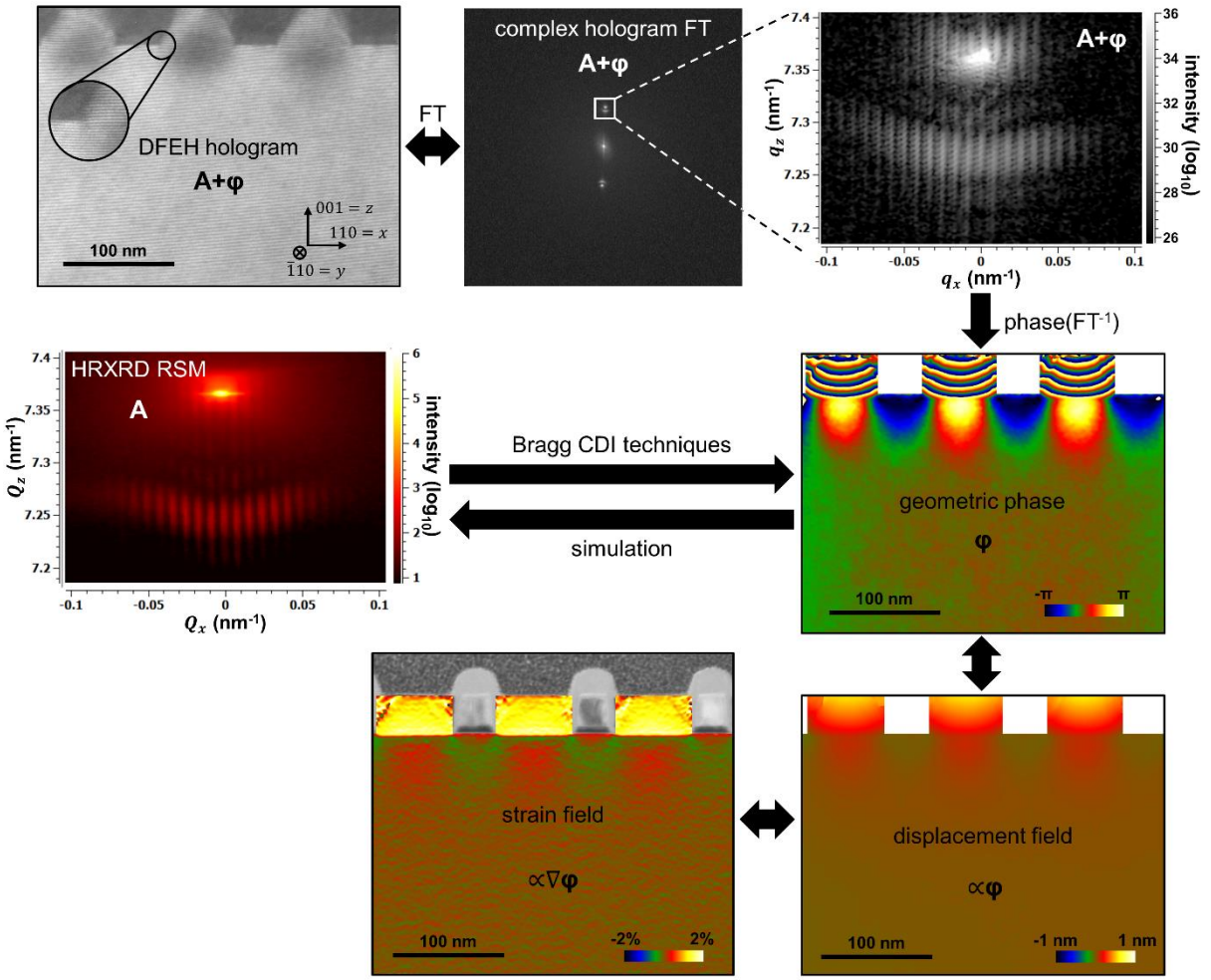

Figure 6: Description of how the fields (geometric phase, displacement and strain) are obtained from DFEH and HRXRD measurements and similarity between the hologram FT and the HRXRD RSM. Information content about the amplitude (A) and phase (φ) of the diffracted beam is indicated.